materials

MDPI

Article

Chirality and Magnetocaloricity in $GdFeTeO_6$ as Compared to $GdGaTeO_6$

Elena Zvereva [1,†], Tatyana Vasilchikova [1], Maria Evstigneeva [2], Angelica Tyureva [2], Vladimir Nalbandyan [2], João Gonçalves [3], Paolo Barone [4], Alessandro Stroppa [5] and Alexander Vasiliev [1,6,*]

1 Department of Low Temperature Physics and Superconductivity, Physics Faculty, Lomonosov Moscow State University, 119991 Moscow, Russia; t_vasilchikova@yahoo.com
2 Department of Chemistry, Southern Federal University, 344090 Rostov-on-Don, Russia; maevstigneeva@gmail.com (M.E.); tyureva.lika@mail.ru (A.T.); vbn@sfedu.ru (V.N.)
3 Department of Physics and CICECO, University of Aveiro, 3810-193 Aveiro, Portugal; joaonsg@ua.pt
4 Consiglio Nazionale delle Ricerche, Institute for Superconducting and Innovative Materials and Devices (CNR-SPIN), Area della Ricerca di Tor Vergata, Via del Fosso del Cavaliere 100, I-00133 Rome, Italy; paolo.barone@spin.cnr.it
5 Consiglio Nazionale delle Ricerche, Institute for Superconducting and Innovative Materials and Devices (CNR-SPIN), c/o Department of Physical and Chemical Sciences, University of L'Aquila, Via Vetoio Coppito, I-67100 L'Aquila, Italy; alessandro.stroppa@spin.cnr.it
6 Quantum Functional Materials Laboratory, National University of Science and Technology "MISiS", 119049 Moscow, Russia
* Correspondence: anvas2000@yahoo.com
† Deceased.

check for updates

Citation: Zvereva, E.; Vasilchikova, T.; Evstigneeva, M.; Tyureva, A.; Nalbandyan, V.; Gonçalves, J.; Barone, P.; Stroppa, A.; Vasiliev, A. Chirality and Magnetocaloricity in $GdFeTeO_6$ as Compared to $GdGaTeO_6$. *Materials* **2021**, *14*, 5954. https://doi.org/10.3390/ma14205954

Academic Editor: Aivaras Kareiva

Received: 13 September 2021
Accepted: 29 September 2021
Published: 10 October 2021

Abstract: $GdFeTeO_6$ and $GdGaTeO_6$ have been prepared and their structures refined by the Rietveld method. Both are superstructures of the rosiaite type (space group $P\bar{3}1c$). Their thermodynamic properties have been investigated by means of magnetization M and specific heat C_p measurements, evidencing the formation of the long-range antiferromagnetic order at T_N = 2.4 K in the former compound and paramagnetic behavior down to 2 K in the latter compound. Large magnetocaloric effect allows considering $GdFeTeO_6$ for the magnetic refrigeration at liquid hydrogen stage. Density functional theory calculations produce estimations of leading Gd–Gd, Gd–Fe and Fe–Fe interactions suggesting unique chiral 120° magnetic structure of Fe^{3+} (S = 5/2) moments and Gd^{3+} (J = 7/2) moments rotating in opposite directions (clockwise/anticlockwise) within weakly coupled layers of the rosiaite type crystal structure.

Keywords: chirality; magnetocaloricity; metaloxide

1. Introduction

Both classical and quantum spin systems of reduced dimensionality host a plethora of exotic magnetic ground states, including spin liquids and peculiar long-range ordered patterns [1,2]. The layered crystal structure of the rosiaite type, AB_2O_6, can be considered as an ideal playground to study the low-dimensional and frustrated magnetism. It is organized by diluted triangular A and dense honeycomb B layers alternating along the trigonal axis c [3]. In case of the A position being occupied by the divalent transition metal ions (M = Mn, Co, Ni), the long-range antiferromagnetic (AFM) order takes place at low temperatures in both MAs_2O_6 arsenates [4] and MSb_2O_6 antimonates [5]. Exceptionally, $CuSb_2O_6$ [5] does not order down to 1.5 K, while $PdAs_2O_6$ orders at an unusually high Néel temperature 140 K [6]. The couple of pentavalent cations in the B layer can be substituted by a combination of tetravalent and hexavalent cations, as is the case of $MnSnTeO_6$ [7].

The A position in the rosiaite structure can be taken also by a trivalent rare-earth metal [8–13] or bismuth [14]. Simultaneously, in accord with charge compensation, half of B positions can be occupied by a trivalent cation (e.g., Cr^{3+} or Fe^{3+}), and another half by Te^{6+}

ions. Concerning magnetic properties, it is known that all $RCrTeO_6$ studied (R = Y, La, Tb, Er, Gd, and Bi) experience the antiferromagnetic transition at low temperatures [11,12,14]. Paramagnetic behavior down to 3 K was observed in $LaFeTeO_6$ [10] and $GdFeTeO_6$ [13], albeit in the latter case it has been anticipated that this compound experiences ferrimagnetic order at lower temperature.

It is well known that in two dimensions, the triangular lattice antiferromagnet in the Ising limit remains disordered at all temperatures. In the Heisenberg limit, the problem of frustration is lifted by 120° arrangement of magnetic moments, which is the essence of Yafet–Kittel model [15]. The magnetic subsystem of $GdFeTeO_6$ is comprised by basically isotropic Gd^{3+} ($J = 7/2$) and Fe^{3+} ($S = 5/2$) ions. It opens the way to unique clockwise/anticlockwise 120° antiferromagnetic structure in case of appreciable *f*–*d* interaction. The reported bond lengths in $GdFeTeO_6$ [13] differ from the corresponding sums of ionic radii [16] by 0.16, 0.24 and 0.29 Å for Gd–O, Fe–O and Te–O, respectively. We report here the preparation, correctly refined crystal structure and detailed experimental and theoretical study of magnetic properties of $GdFeTeO_6$ in comparison with its analogue containing diamagnetic Ga^{3+} in place of Fe^{3+}.

2. Experimental

2.1. Sample Preparation, Phase Analysis and Structural Studies

Polycrystalline samples of $GdFeTeO_6$ and $GdGaTeO_6$ were prepared by solid-state reactions (see Electronic Supplementary Material, ESM, for details). Reasonable agreement of the hexagonal lattice parameters for $GdFeTeO_6$ prepared by different methods, even in the presence of foreign phases (Table S1 of ESM), suggests that the compound does not have any extended homogeneity range.

XRD studies were performed in CuK_α radiation using an ARL X'tra diffractometer, Thermo Scientific, Switzerland, in the Bragg–Brentano geometry, equipped with a solid-state Si(Li) detector. Lattice parameters were refined using CELREF 3 (J. Laugier and B. Bochu), with angular corrections by corundum (NIST SRM 676) as an internal standard. To reduce effect of grain orientation, the samples for the XRD profile analysis were mixed with amorphous powder (instant coffee). The structures were refined with the GSAS + EXPGUI suite [17,18].

2.2. Physical Measurements

Magnetization M and specific heat C_p were studied using various options of Physical Properties Measurements System PPMS–9T, Quantum Design, San Diego, CA, USA.

3. Results and Discussion

3.1. Crystal Structures of $GdMTeO_6$ (M = Fe, Ga)

For the structure analysis, we used a single-phase light yellow $GdFeTeO_6$ powder prepared by solid-state reaction at a final temperature of 830 °C and white $GdGaTeO_6$ powder prepared at 950 °C. The latter contained trace amounts of Ga_2O_3 and an unknown phase, and this may explain somewhat lower accuracy of its structural data (see below). The crystal structures were successfully refined starting from the structural model of $LaFeTeO_6$ [10].

Experimental and calculated XRD profiles are compared in Figure 1; experimental and refinement details, crystallographic data, atomic coordinates and displacement parameters are reported in Tables S2–S4 and Figure S2 of ESM, and bond lengths, bond angles and bond valence sums (BVS), in Table 1. The Crystallographic information files (CIF) are supplied as Supplementary Material. The data for $GdFeTeO_6$ have been deposited at the Cambridge Crystallographic Data Centre as CCDC 2002460.

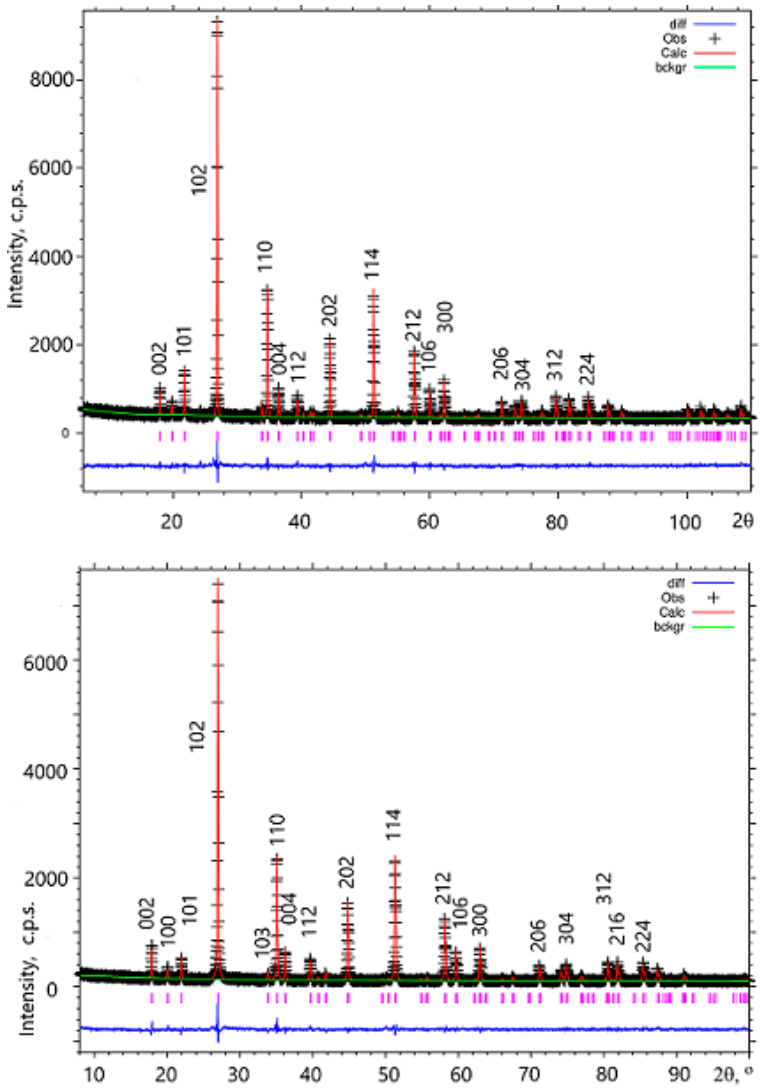

Figure 1. Results of the Rietveld refinement for $GdFeTeO_6$ (**top**) and $GdGaTeO_6$ (**bottom**). Crosses, experimental data; red line, calculated profile; bottom blue line, difference profile; vertical bars, Bragg angles.

Table 1. Lattice parameters, bond lengths (Å), sums of ionic radii [16], bond valence [19] sums (BVS) and bond angles in $GdMTeO_6$ (M = Fe, Ga).

		$GdFeTeO_6$	**$GdGaTeO_6$**
a, Å		5.16556(5)	5.11096(6)
c, Å		9.85231(14)	9.91922(17)
c/a		1.907	1.941
Distances/sum of radii/BVS	Gd-O	2.3283(10) × 6/2.30/2.73	2.280(10) × 6/2.30/3.06
	M-O	2.0141(9) × 6/2.005/3.01	1.929(10) × 6/1.98/3.43
	Te-O	1.9301(8) × 6/1.92/5.88	2.029(10) × 6/1.92/5.02
O: BVS		1.94	1.92
Angles (°)	Gd-O-Te	130.31(4)	126.8(5)
	Te-O-M	98.22(4)	96.4(4)
	M-O-Gd	125.78(4)	132.4(5)

Table 1. *Cont.*

		$GdFeTeO_6$	$GdGaTeO_6$
	Sum for O	354.3	355.6
	O-Gd-O	88.0–92.0	86.2–93.8
	O-M-O	79.7–94.2	86.2–91.7
	O-Te-O	83.9–92.1	81.0–94.3

For the Fe compound, possible Te/Fe inversion was investigated, but the refined degree of inversion, 0.02, was within experimental accuracy and, therefore, was neglected. The structures are very similar and Figure 2 effectively represents both of them. Bond lengths agree with the corresponding sums of ionic radii (less accurately for M = Ga), and calculated BVS are also reasonable. Each oxygen anion has an almost planar environment, with the sum of the three bond angles being close to 360° (Table 1).

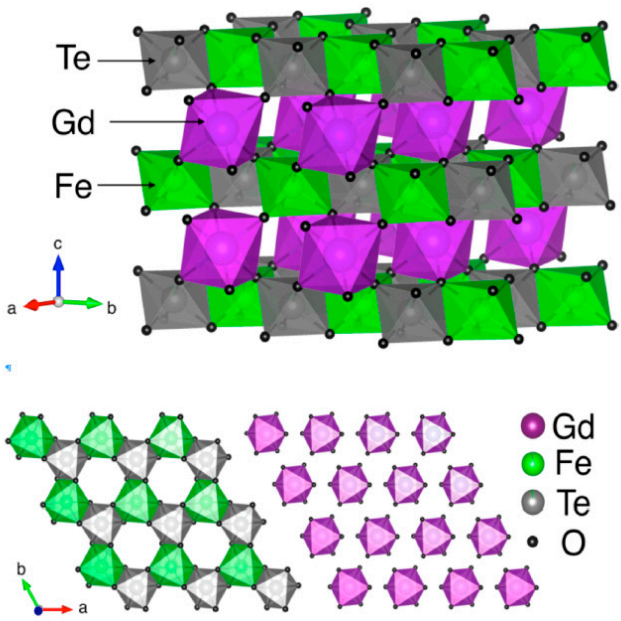

Figure 2. Upper panel: Polyhedral presentation of the crystal structure of $GdFeTeO_6$, Violet, green, grey and black spheres are Gd, Fe, Te and O ions, respectively. Lower panel: magnetoactive layer of Fe and Te ions, and Gd layer. A three-dimensional visualization system VESTA [20] for electronic and structural analysis has been used for the presentation of crystal structure.

3.2. Basic Properties

The temperature dependences of magnetic susceptibility $\chi = M/B$ in both $GdFeTeO_6$ and $GdGaTeO_6$ taken at B = 0.1 T are shown in the left panel of Figure 3. Note that no difference between data obtained within field-cooled and zero-field-cooled protocols has been observed signaling absence of any impurity-driven or spin-glass effects. In a wide temperature range, both compounds evidence paramagnetic behavior following basically the Curie law $\chi = C/T$. The Curie constants C are 11.96 emu K/mol for $GdFeTeO_6$ and 7.58 emu K/mol for $GdGaTeO_6$ in full correspondence with expectations for Gd^{3+} ($J = 7/2$) and Fe^{3+} ($S = 5/2$) magnetic moments. Straight inverse susceptibility curves, $\chi^{-1}(T)$, point to the absence of any magnetic frustration effects inherent to triangular systems. While $GdGaTeO_6$ remains paramagnetic down to 2 K, the $\chi(T)$ curve in $GdFeTeO_6$ evidences the kink ascribed to antiferromagnetic phase transition at T_N = 2.4 K. This part of the $\chi(T)$ curve is enlarged in the inset to the left panel of Figure 3. The kink at 2.4 K is readily suppressed by an external magnetic field. The field dependences of magnetization $M(B)$ in $GdFeTeO_6$ and $GdGaTeO_6$ taken at 2 K are shown in the right panel of Figure 3. In

both compounds, the magnetization reaches the saturation values, albeit the shape of $M(B)$ curve in $GdFeTeO_6$ differs from that in $GdGaTeO_6$, presumably due to f–d interactions which result in magnetic long-range order.

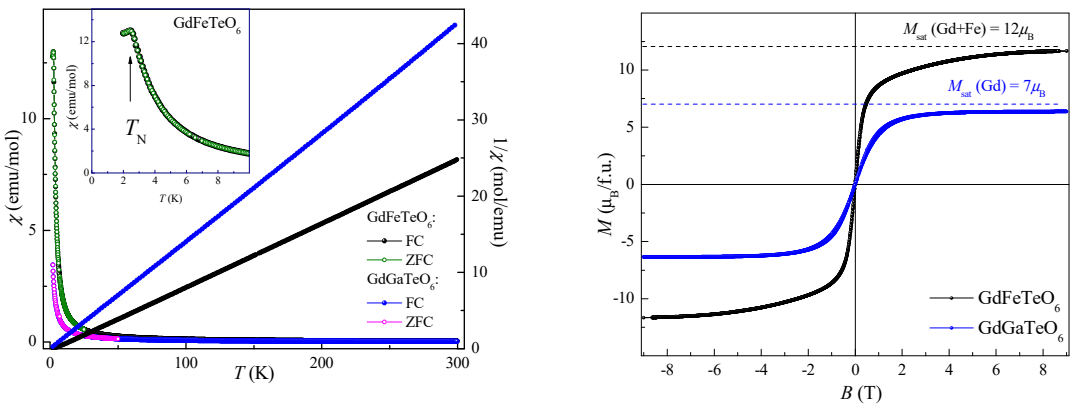

(**a**) (**b**)

Figure 3. (**a**) The temperature dependences of magnetic susceptibility χ in $GdFeTeO_6$ and $GdGaTeO_6$ at B = 0.1 T (left ordinate) and inverse susceptibility $1/\chi$ (right ordinate). The inset enlarges the low temperature part of $\chi(T)$ curve for $GdFeTeO_6$. (**b**) The field dependences of magnetization $M(B)$ in $GdFeTeO_6$ and $GdGaTeO_6$ at 2 K.

The evidence for the magnetic phase transition in $GdFeTeO_6$ was further obtained from the specific heat data, as shown in the left panel of Figure 4. The $C_p(T)$ curve taken in the absence of magnetic field evidences sharp λ-type anomaly at T_N = 2.4 K. The data well above the transition temperature were used to estimate the phonon background $C_{lattice}$ in $GdFeTeO_6$ using the Debye model, as shown by the solid line in Figure 4. No such anomaly has been detected down to 2 K in $GdGaTeO_6$; however, a slight upturn of specific heat at lowest temperatures should be noted which can be considered as an indication for the forthcoming low-temperature magnetic phase transition. An external magnetic field rapidly suppresses the λ-peak in $C_p(T)$ curve, but the Schottky-type anomaly appears at elevated temperatures. This anomaly is associated with the Zeeman splitting of magnetic levels in both gadolinium and iron ions. It shifts to higher temperatures with increasing magnetic field. Similarly, the Zeeman splitting of gadolinium levels in $GdGaTeO_6$ results in the appearance of pronounced Schottky anomaly, as shown in the right panel of Figure 4.

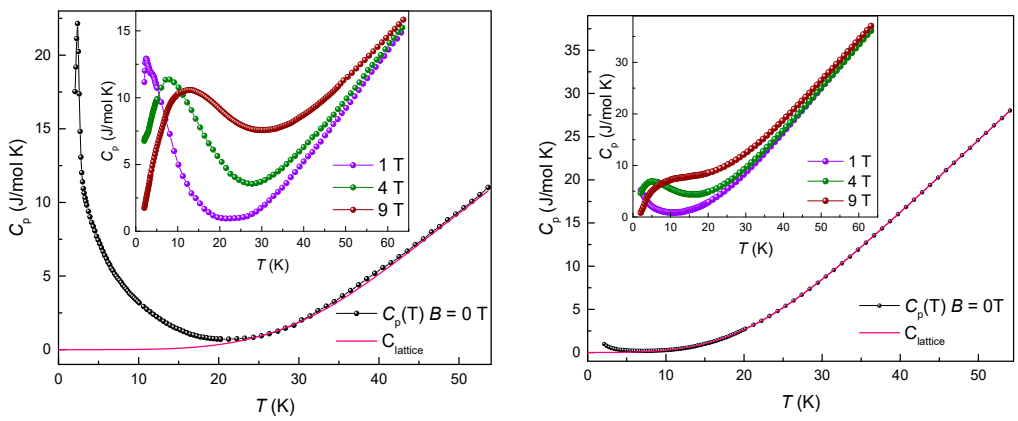

(a) (b)

Figure 4. The temperature dependences of the specific heat C_p in $GdFeTeO_6$ (**a**) and $GdGaTeO_6$ (**b**). The solid lines represent the Debye fitting of the phonon contributions. The insets show $C_p(T)$ curves taken in various magnetic fields.

3.3. Magnetocaloric Effect

The magnetocaloric effect in $GdFeTeO_6$ was estimated from the specific heat data $C_p(T, B)$ at various magnetic fields. The lattice contribution $C_{lattice}$ has been subtracted from the total specific heat $C_p(T, B)$ to estimate the magnetic entropy S_m(T), as shown in the left panel of Figure 5. The magnetic entropy change $\Delta S_M(T, \Delta B)$ has been calculated as $\Delta S_M(T, \Delta B) = S_m(T, B) - S_m(T, 0)$. The adiabatic change of the magnetic field from B_1 to B_2 causes not only change in the magnetic entropy, but also alteration of the sample temperature $\Delta T_{ad} = T_2 - T_1$, which can be determined by the adiabatic condition $S(T, B_1) = S(T + \Delta T, B_2)$. Thus, ΔT_{ad} has been calculated from the zero-field $C_p(T)$ and $\Delta S_M(T, \Delta B)$ data with the use of equation:

$$\Delta T(T, \Delta B) = T\left[\exp\left(-\frac{dS_M(T, \Delta B)}{C_p(T, 0)}\right) - 1\right] \quad (1)$$

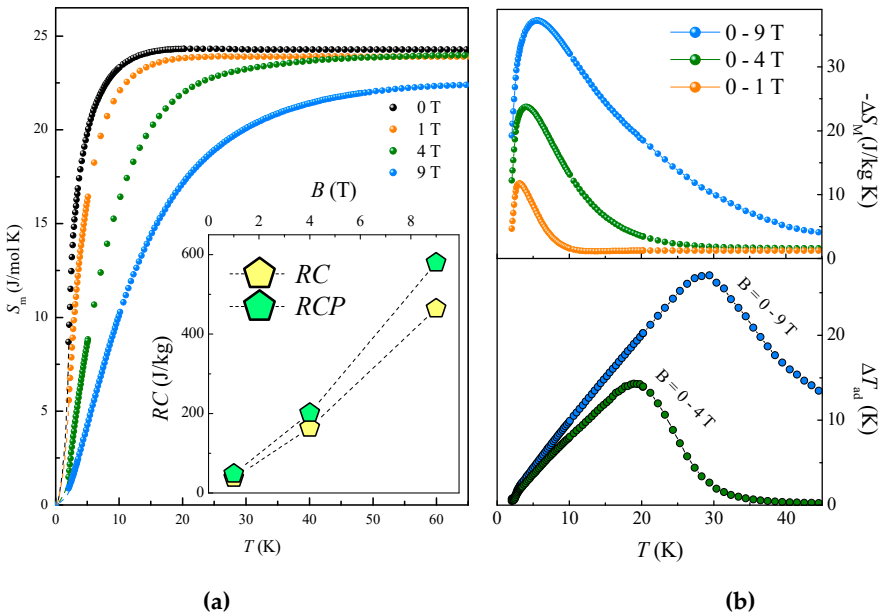

Figure 5. The temperature dependence of the magnetic entropy S_M in various magnetic fields. The inset shows the field dependences of the refrigerant capacity *RC* and the relative cooling power *RCP* (**a**). The magnetic entropy ΔS_M and adiabatic temperature change ΔT_{ad} (**b**).

Right panels of Figure 5 show both ΔS_M and ΔT_{ad} sets of data in $GdFeTeO_6$ as a function of temperature for the various external magnetic fields. These curves demonstrate a broad peak for both quantities, with the width increasing at higher magnetic fields. The maximum value $-\Delta S_M{}^{max}$ is 35.3 J/kg K for the field change of 0–9 T. This result agrees with the previous data for $\Delta S_M(T, \Delta B)$ derived from an isothermal process of magnetization using the Maxwell relations. The temperature change, ΔT_{ad}, is 27 K at 9 T reaching liquid hydrogen temperatures.

The magnetocaloric study is completed by the estimation of refrigeration properties for $GdFeTeO_6$. The results for the refrigerant capacity (RC) and the relative cooling power (RCP) vs. applied magnetic field are shown in the inset to the right panel of Figure 5. The RC and the RCP are defined as

$$RC = \int_{T_1}^{T_2} |\Delta S_M dT|, RCP = |\Delta S_M^{max}| \times |\delta T_{FWHM}| \quad (2)$$

where T_1 and T_2 represent the temperatures corresponding to the half maximum of $\Delta S_M(T)$ curve, $\Delta S_M{}^{max}$ is the maximum of ΔS_M value, and δT_{FWHM} is the width at half maximum

(FWHM) of $\Delta S_M(T)$ curve. Note that similarly large magnetocaloric effect has been recently reported for another *f*-*d* oxide of rosiaite-type $GdCrTeO_6$ [12].

3.4. Density Functional Calculations

Density functional theory calculations [21,22] were performed to study the magnetic interactions by determining the exchange interactions. We considered both Perdew–Burke–Ernzerhof (PBE + U) [23,24] and Heyd–Scuseria–Ernzerhof (HSE) [25,26] exchange correlation functionals. For the PBE + U calculations, the choice of U for the f electrons is subtle since different values have been deemed a reasonable choice for each specific material. For example, in elemental Gd [27] and Gd monopnictides [28], a $U_{eff} = U\text{-}J$ value of 6 eV has been used, but in some transition metal oxides a lower value of 4 eV has been found more appropriate for the f electrons of Gd and Dy [29,30]. In the previous study for this compound, a value of U_{Gd} = 6 eV has been used [13]. However, we found that the energy difference between different magnetic configurations is very sensitive to U_{Gd}. Therefore, previous calculations for similar compounds must be considered with care with respect to the choice of the U parameter. In order to avoid ambiguities in the choice of U correction, we have used the HSE functional calculations as a benchmark. The energy differences are more sensitive to U_{Gd}, with a value U_{Gd} close to 2.09 eV needed, but much less sensitive to U_{Fe}, with 4 U_{Fe} = 5 eV producing similar energy differences. Nevertheless, there is no single combination of U values which can reproduce all the HSE energy differences between magnetic states, which prompted us to adopt the latter approach also in the estimate of exchange interactions. This is probably due to the fact that while HSE affects both *p*- and *d*-states, the U correction affects mainly the *d*-states [31].

We considered the 2 × 1 × 1 supercell in order to estimate the pairwise exchange interactions. Four Gd and four Fe atoms are considered, hence 9 possible AFM states, since both Fe and Gd can have three different AFM spin arrangements. We considered the FM, the nine AFM states and five additional FiM states, both for HSE and PBE + U, with U_{Gd} = 2.09, U_{Fe} = 5 eV, which was found to be a reasonable compromise to reproduce the HSE energies. We evaluated the exchange interactions by mapping the first-principles magnetic energies to the Heisenberg model:

$$H = \frac{1}{2}\sum_{i,j} J_{i,j}\vec{S}_i \Delta \vec{S}_j \tag{3}$$

and performing multiple linear regression with least-squares fitting. Gd–Gd interactions were found to be negligible, and the magnetic energies can be well reproduced in a minimal model comprising only Fe–Fe and nearest-neighbor Gd-Fe interactions. The third nearest-neighbor out-of-plane Fe–Fe interaction was found to be important for improving the linear regression, even though the distance between involved Fe atoms is quite large; this exchange is in fact mediated by the same bridging atoms involved in the other Fe–Fe exchanges, occurring on a Fe–O–Gd–O–Fe path. The estimated values of the exchange interactions for PBE + U and HSE approaches are shown in Table 2. The interactions within HSE are generally reduced in comparison with PBE + U, with the main difference being a much smaller Fe–Fe in-plane interaction, and the sign of the next-nearest-neighbor $J_{Fe-Fe}^{out-of-plane}$, which turned out to be the only ferromagnetic interaction at the HSE or PBE + U levels. The in-plane AFM Fe–Fe interaction is known to lead to a (classical) co-planar three-sublattice "120-degree" state within each Fe-layer, while the Gd–Fe AFM interaction, mediating an inter-layer coupling between Fe layers, would instead promote a ferrimagnetic state with antiparallel Fe and Gd spins, and the third nearest-neighbor $J_{\mathrm{Fe-Fe}}^{nnnout-of-plane}$ would instead favor AFM configurations of Fe spins. Such a fierce competition of magnetic exchange interactions combined with their weakness in magnitude is compatible with the low critical temperature observed in the system. Indeed, we used the estimated interactions to predict the critical temperature within a classical Monte Carlo approach. Using a Metropolis algorithm for an 18 × 18 × 12 cell, we found cusps in the specific heat and magnetic

susceptibility signaling a transition at T_N ~ 2.6 K (5 K) for exchange parameters evaluated within the HSE (PBE + U) approach, with no net magnetization developing in the ordered phase, in good agreement with the experimental estimates.

Table 2. Effective and renormalized (with J_{Gd} = 7/2, S_{Fe} = 5/2) exchange constants (meV) obtained by fitting to the PBE + U (U_{Gd} = 2.09, U_{Fe} = 5 eV) and HSE energies.

	Effective Exchange $J_{ij}^{e} = S_i S_j J_{ij}$ (meV)		**J_{ij} for J_{Gd} = 7/2, S_{Fe} = 5/2 (meV)**	
	PBE + U	**HSE**	**PBE + U**	**HSE**
$J_{Fe-Fe}^{in-plane}$	−0.4683	−0.0356	−0.0749	−0.0057
$J_{Fe-Fe}^{out-of-plane}$	−0.0263	0.0169	−0.0042	0.0027
J_{Fe-Gd}	−0.0382	−0.0993	−0.0044	−0.0113
$J_{Fe-Fe}^{nnout-of-plane}$	−0.1831	−0.1182	−0.0293	−0.0189

The HSE (PBE + U) calculated local magnetic moments have absolute values of approximately 6.92, 4.25, 0.00, and 0.10 (6.97, 4.29, 0.01, and 0.09) μ_B, for Gd, Fe, Te, and O, respectively, irrespective of the magnetic order considered, consistent with Gd^{3+} (J = 7/2) and Fe^{3+} (S = 5/2) ions, in agreement with the susceptibility measurements.

3.5. Discussion

The crystal structure of both $GdFeTeO_6$ and $GdGaTeO_6$ is a superstructure (space group $P\bar{3}1c$) of the rosiaite AB_2O_6 [3] due to the doubling of the c parameter associated with the alternating Fe/Te or Ga/Te along the principal axis. Thermodynamic measurements evidence the long-range magnetic order at T_N = 2.4 K in $GdFeTeO_6$ and paramagnetic behavior down to 2 K in $GdGaTeO_6$. $GdFeTeO_6$ possesses excellent magnetocaloric properties. For a magnetic field change of 9 T at 2 K, the values of entropy change $-\Delta S_M(T)$ = 35.3 J/kg K and adiabatic temperature alteration ΔT_{ad} = 27 K are obtained, as well as relative cooling power 580 J/kg and refrigerant capacity 465 J/kg. This makes $GdFeTeO_6$ attractive for the working body of low-temperature magnetic refrigerator devices. With the intensification of research at helium temperatures, the problem of cooling the current leads of superconducting solenoids and reaching ultralow temperatures becomes increasingly urgent [32–37].

The presence of gadolinium in the structure of $GdFeTeO_6$ precludes determination of its magnetic structure using neutron scattering methods. However, the absence of the magnetic order in $GdGaTeO_6$ evidences the weakness of the Gd–Gd interactions. Moreover, no long-range order has been detected in $LaFeTeO_6$, pointing to the weakness of interlayer Fe–Fe interactions [10]. $GdFeTeO_6$ represents a unique system which orders due to interlayer f–d interactions. The absence of spontaneous magnetization in the magnetically ordered phase of this compound excludes any ferrimagnetic arrangement of Gd^{3+} and Fe^{3+} magnetic moments [13]. The only solution compatible with the absence of any frustration effects in magnetic susceptibility seems to be 120° structure of iron moments within B layers (say, clockwise) and 120° structure of gadolinium moments within A layers (say, anticlockwise), as shown in Figure 6. In the first principle calculations, this structure is of the lowest energy, but the energy difference with other configurations is very small, about 0.01 meV per formula unit. In our knowledge, the proposed chiral–antichiral magnetic structure is unique, deserving some kind of experimental verification.

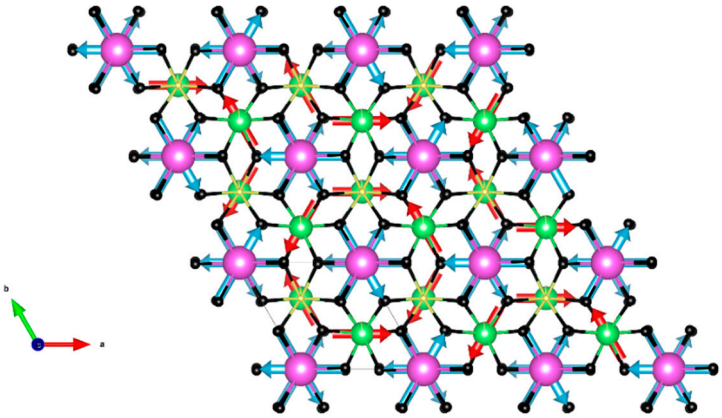

Figure 6. The ball-and-stick representation [20] of the crystal structure of $GdFeTeO_6$. Purple, green, gray and black spheres are Gd, Fe, Te and O ions, respectively. Blue and pink arrows highlight the clockwise and anticlockwise arrangements of spins in different magnetoactive layers.

Supplementary Materials: The following are available online at https://www.mdpi.com/article/10.3390/ma14205954/s1, Figure S1. Comparison of the two XRD patterns of nominal "$GdFeTeO_6$" taken in CuKα radia-tion. Upper panel: Relatively pure phase prepared from oxides for 48 h at 700 °C [5]. Lower pan-el: mixed phase prepared by the semi-wet method for 56 h at 750 °C with three intermediate re-grindings (this work), Figure S2. Correlation between crystal radii [6] of RE^{3+} and hexagonal subcell parameters of $REFeTeO_6$. Red diamonds, a; blue triangles, c/2; RE = La [1, 3, 4], Pr, Nd, Sm [4], and Gd (this work); green circles, same from Reference [5], Figure S3. (a) Effect of changing UGd (eV) for the energy differences of one AFM and 3 FiM states with respect to the FM state. Changes of Gd UGd in the legend, with fixed UFe = 4 eV. (b) Energy difference between FiM1 and FM states. Effect of changing UGd and UFe, and comparison with HSE calculations (black line), Figure S4. The comparison of Monte-Carlo calculations (solid lines) with the experimental tem-perature dependencies of magnetic susceptibility χ(T) (left panel) and specific heat Cp(T) (right panel), Table S1. Phase analysis results and hexagonal lattice parameters of $GdFeTeO_6$ samples prepared by various methods, Table S2. Details of the data collection and structure refinement, Table S3. Atomic coordinates and displacement parameters in $GdFeTeO_6$, space group $P\bar{3}1c$, Table S4. Atomic coordinates and displacement parameters in $GdGaTeO_6$, space group $P\bar{3}1c$.

Author Contributions: Conceptualization, E.Z., P.B., A.V.; methodology, V.N.; investigation, M.E., A.T., T.V. and J.G.; writing—original draft preparation, E.Z., V.N. and A.S. All authors have read and agreed to the published version of the manuscript.

Funding: This work has been supported by the grant 18-03-00714 from the Russian Foundation for Basic Research (for V.N., E.Z., and M.E.) and Grant-in-Aid 00-15 from the International Centre for Diffraction Data (for V.N. and M.E.); A.V. acknowledges the support of experimental study by Megagrant Program of the Government of Russian Federation through the project 075–15–2021-604. A.S. and J.G. thanks HPC-Europa3 for funding.

Data Availability Statement: The data presented in this study are available in supplementary material.

Acknowledgments: J.G. and A.S. gratefully acknowledge HPC-Europa3 Transnational Access programme HPC-EUROPA3 (INFRAIA-2016-1-730897, HPC17T6HD5), with the support of the EC Research Innovation Action under the H2020 Programme. J.G. gratefully acknowledges the computer resources/technical support provided by CINECA, and the kind hospitality by CNR-SPIN c/o Department of Chemical and Physical Science of University of L'Aquila (Italy) during the visiting period from 3 November 2019 to 21 December 2019 and from 7 January 2020 to 15 February 2020.

Conflicts of Interest: The authors declare no conflict of interest.

References

1. Vasiliev, A.; Volkova, O.; Zvereva, E.; Markina, M. Milestones of low-D quantum magnetism. *NPJ Quantum Mater.* **2018**, *3*, 18. [CrossRef]
2. Vasil'ev, A.N.; Markina, M.M.; Popova, E.A. Spin gap in low-dimensional magnets. *Low Temp. Phys.* **2005**, *31*, 203–223. [CrossRef]
3. Basso, R.; Lucchetti, G.; Zefiro, L.; Palenzona, A. Rosiaite, $PbSb_2O_6$, a new mineral from the Cetine mine, Siena, Italy. *Eur. J. Miner.* **1996**, *8*, 487–492. [CrossRef]
4. Nakua, A.; Greedan, J. Structural and magnetic properties of transition-metal arsenates, AAs_2O_6, A = Mn, Co, and Ni. *J. Solid State Chem.* **1995**, *118*, 402–411. [CrossRef]
5. Nikulin, A.Y.; Zvereva, E.A.; Nalbandyan, V.B.; Shukaev, I.L.; Kurbakov, A.I.; Kuchugura, M.D.; Raganyan, G.V.; Popov, Y.V.; Ivanchenko, V.D.; Vasiliev, A.N. Preparation and characterization of metastable trigonal layered MSb_2O_6 phases (M = Co, Ni, Cu, Zn, and Mg) and considerations on $FeSb_2O_6$. *Dalton Trans.* **2017**, *46*, 6059–6068. [CrossRef] [PubMed]
6. Reehuis, M.; Saha-Dasgupta, T.; Orosel, D.; Nuss, J.; Rahaman, B.; Keimer, B.; Andersen, O.; Jansen, M. Magnetic properties of $PdAs_2O_6$: A dilute spin system with an unusually high Neel temperature. *Phys. Rev. B* **2012**, *85*, 115118. [CrossRef]
7. Nalbandyan, V.; Evstigneeva, M.; Vasilchikova, T.; Bukhteev, K.; Vasiliev, A.; Zvereva, E. Trigonal layered rosiaite-related antiferromagnet $MnSnTeO_6$: Ion-exchange preparation, structure and magnetic properties. *Dalton Trans.* **2018**, *47*, 14760–14766. [CrossRef] [PubMed]
8. Kasper, H.M. $LnCrTeO_6$—A new series of compounds based on the $PbSb_2O_6$ structure. *Mater. Res. Bull.* **1969**, *4*, 33–38. [CrossRef]
9. Lavat, A.; Mercader, C.; Baran, E. Crystallographic and spectroscopic characterization of $LnFeTeO_6$ (Ln = La, Pr, Nd, Sm) materials. *J. Alloys Compd.* **2010**, *508*, 24–27. [CrossRef]
10. Phatak, R.; Krishnan, K.; Kulkarni, N.; Achary, S.; Banerjee, A.; Sali, S. Crystal structure, magnetic and thermal properties of $LaFeTeO_6$. *Mater. Res. Bull.* **2010**, *45*, 1978–1983. [CrossRef]
11. Rao, G.N.; Sankar, R.; Muthuselvam, I.P.; Chou, F.C. Magnetic and thermal property studies of $RCrTeO_6$ (R = trivalent lanthanides) with layered honeycomb sublattices. *J. Magn. Magn. Mater.* **2014**, *370*, 13–17. [CrossRef]
12. Liu, J.; Ouyang, Z.; Liu, X.; Cao, J.; Wang, J.; Xia, Z.; Rao, G. Decoupling of Gd-Cr magnetism and giant magnetocaloric effect in layered honeycomb tellurate $GdCrTeO_6$. *J. Appl. Phys.* **2020**, *127*, 173902. [CrossRef]
13. Lei, D.; Ouyang, Z.; Yue, X.; Yin, L.; Wang, Z.; Wang, J.; Xia, Z.; Rao, G. Weak magnetic interaction, large magnetocaloric effect, and underlying spin model in triangular lattice $GdFeTeO_6$. *J. Appl. Phys.* **2018**, *124*, 233904. [CrossRef]
14. Kim, S.W.; Deng, Z.; Fischer, Z.; Lapidus, S.H.; Stephens, P.W.; Li, M.-R.; Greenblatt, M. Structure and magnetic behavior of layered honeycomb tellurates, BiM(III)TeO_6 (M = Cr, Mn, Fe). *Inorg. Chem.* **2016**, *55*, 10229–10237. [CrossRef] [PubMed]
15. Yafet, Y.; Kittel, C. Antiferromagnetic arrangements in ferrites. *Phys. Rev.* **1952**, *87*, 290–294. [CrossRef]
16. Shannon, R.D. Revised effective ionic-radii and systematic studies of interatomic distances in halides and chalcogenides. *Acta Crystallogr. A* **1976**, *32*, 751–767. [CrossRef]
17. Larson, A.; Von Dreele, R. *General Structure Analysis System (GSAS)*; Report LAUR 86-748; Los Alamos National Laboratory: Los Alamos, NM, USA, 2004.
18. Toby, B. EXPGUI, a graphical user interface for GSAS. *J. Appl. Crystallogr.* **2001**, *34*, 210–213. [CrossRef]
19. Gagné, O.; Hawthorne, F. Comprehensive derivation of bond-valence parameters for ion pairs involving oxygen. *Acta Crystallogr. Sect. B* **2015**, *71*, 562–578. [CrossRef]
20. Momma, K.; Izumi, F. VESTA: A three-dimensional visualization system for electronic and structural analysis. *J. Appl. Crystallogr.* **2008**, *41*, 653–658. [CrossRef]
21. Blöchl, P. Projector augmented-wave method. *Phys. Rev. B* **1994**, *50*, 17953–17979. [CrossRef]
22. Kresse, G.; Furthmüller, J. Efficient iterative schemes for ab initio total-energy calculations using a plane-wave basis set. *Phys. Rev. B* **1996**, *54*, 11169–11186. [CrossRef] [PubMed]
23. Perdew, J.; Burke, K.; Ernzerhof, M. Generalized Gradient Approximation Made Simple. *Phys. Rev. Lett.* **1996**, *77*, 3865–3868. [CrossRef] [PubMed]
24. Dudarev, S.; Botton, G.; Savrasov, S.; Humphreys, C.; Sutton, A. Electron-energy-loss spectra and the structural stability of nickel oxide: An LSDA+U study. *Phys. Rev. B* **1998**, *57*, 1505–1509. [CrossRef]
25. Heyd, J.; Scuseria, G.; Ernzerhof, M. Hybrid functionals based on a screened Coulomb potential. *J. Chem. Phys.* **2003**, *118*, 8207–8215. [CrossRef]
26. Krukau, A.; Vydrov, O.; Izmaylov, A.; Scuseria, G. Influence of the exchange screening parameter on the performance of screened hybrid functionals. *J. Chem. Phys.* **2006**, *125*, 224106. [CrossRef]
27. Kurz, P.; Bihlmayer, G.; Blügel, S. Magnetism and electronic structure of hcp Gd and the Gd (0001) surface. *J. Phys. Condens. Matter* **2002**, *14*, 6353–6371. [CrossRef]
28. Duan, C.-G.; Sabiryanov, R.; Mei, W.; Dowben, P.; Jaswal, S.; Tsymbal, E. Electronic, magnetic and transport properties of rare-earth monopnictides. *J. Phys. Condens. Matter* **2007**, *19*, 315220. [CrossRef]
29. Stroppa, A.; Marsman, M.; Kresse, G.; Picozzi, S. The multiferroic phase of $DyFeO_3$: An ab initio study. *New J. Phys.* **2010**, *12*, 093026. [CrossRef]
30. Zhao, H.; Bellaiche, L.; Chen, X.; Íñiguez, J. Improper electric polarization in simple perovskite oxides with two magnetic sublattices. *Nat. Commun.* **2017**, *8*, 14025. [CrossRef]
31. Kümmel, S.; Kronik, L. Orbital-dependent density functionals: Theory and applications. *Rev. Mod. Phys.* **2008**, *80*, 3–60. [CrossRef]

32. Tian, Y.; Ouyang, J.L.; Hiao, H.B.; Zhang, Y.K. Structural and magnetocaloric properties in the aeschynite type $GdCrWO_6$ and $ErCrWO_6$ oxides. *Ceram. Int.* **2021**, *47*, 29197–29204. [CrossRef]
33. Wang, X.; Wang, Q.; Tang, B.Z.; Peng, P.; Xia, L.; Ding, D. Large magnetic entropy change and adiabatic temperature rise of a ternary $Gd_{34}Ni_{33}Al_{33}$ metallic glass. *J. Rare Earths* **2021**, *39*, 998–1002. [CrossRef]
34. Liu, T.; Liu, X.Y.; Gao, Y.; Jin, H.; He, J.; Sheng, X.L.; Jin, W.T.; Chen, Z.Y.; Li, W. Significant inverse magnetocaloric effect induced by quantum criticality. *Phys. Rev. Res.* **2021**, *3*, 033094. [CrossRef]
35. Shi, J.H.; Seehra, M.S.; Dang, Y.L.; Suib, S.L.; Jain, M. Comparison of the dielectric and magnetocaloric properties of bulk and film of $GdFe_{0.5}Cr_{0.5}O_3$. *J. Appl. Phys.* **2021**, *129*, 243904. [CrossRef]
36. Shi, J.H.; Sauyet, T.; Dang, Y.L.; Suib, S.L.; Seehra, M.; Jain, M. Structure-property correlations and scaling in the magnetic and magnetocaloric properties of $GdCrO_3$ particles. *J. Phys. Condens. Matter* **2021**, *33*, 205801. [CrossRef] [PubMed]
37. Tokiwa, Y.; Bachus, S.; Kawita, K.; Jesche, A.; Tsirlin, A.A.; Gegenwart, P. Frustrated magnet for adiabatic demagnetization cooling to milli-Kelvin temperatures. *Commun. Mater.* **2021**, *2*, 42. [CrossRef]